A modular cable robot for inspection and light manipulation on celestial bodies

S. Seriani [a,1], P. Gallina [a], A. Wedler [b]

[a] University of Trieste, Department of Engineering and Architecture, Italy
[b] Robotik und Mechatronik Zentrum, Deutsches Zentrum für Luft- und Raumfahrt e.V. (DLR), Germany

ARTICLE INFO

Accepted 20 March 2016

Keywords:
Space exploration
Robotics
Cable robot
Modular robotics
Workspace
Stability

ABSTRACT

Planetary exploration has been carried out with solitary probes since the nineteen-sixties; on the other hand, the newly emerging paradigm for robotic exploration shows multi-expertize, complex modular systems as necessary for efficient and thorough activities. In this paper we propose a modular Cable Driven Parallel Robot (CDPR) that is deployed by a rover, which can take advantage of its large workspace for tasks as inspection or light manipulation. While the general deployment procedure is described, focus is given on the CDPR; a model for the pseudostatics of the robot is formulated, as well as an analysis on its modules stability. The workspace is then characterized using appropriate metrics. Results show that a 1 Kg payload for the end-effector is effectively feasible with substantial margin for an equilateral triangular workspace of 10 m side. Finally, several possible practical applications are illustrated.

1. Introduction

The exploration of planets and other celestial bodies has been, up to this point in history, carried out by the use of small, solitary, one-package probes [1,2]. Since the first soft landing performed by the Soviet's Luna 9 in 1966 on the Moon, many landers have been deployed all around the solar system, e.g. Mars [3], Venus, even Jupiter's moon Titan with ESA's Huygens probe [4] in 2005, or, more recently, the partially successful landing of ESA's probe Philae [5] on comet 67P/Churyumov–Gerasimenko. A subset of these probes are the so-called rovers, robotic vehicles designed to travel across the surface of planets or, more generally, unexplored, and possibly hostile, environments. Notable examples are Lunokhod 1, deployed on the moon in 1970, which kept operating for 11 months, the mars rovers MER-A and MER-B, the latter still in operation after more than 11 years from its landing, and finally the most recent Mars Science Laboratory (MSL) rover [6]. Future planned rovers include ISRO's Chandrayaan-2 [7], ESA's ExoMars [8] and Mars 2020 Rover Mission from NASA [9]. As it is clear from reviewing all these missions, the focus is on the scientific payload that is on-board the rover. This calls the robot to be conceived primarily as a mobility and support structure for the several instruments that need to probe the environment in different locations. This rationale results in a system that needs to be as self-contained as possible, to be efficient and to save weight. A partial deviation in principle is represented by landers made by an autonomous base and a rover. An example is NASA's Sojourner, part of the Mars Pathfinder mission [10], in 1996–7, or the recent Chang'e 3, with its partially successful rover Yutu [11], in 2013.

The design of rovers has thus been geared towards mere carriers of scientific instruments. Indeed, modularity in its broad sense has seen, up to now, extremely limited practical development in the field of space exploration, mainly for the mentioned lack of necessity. In the last decade, though, with the prospect of entering into a new phase of exploration – especially of Mars and the Moon – a new paradigm is starting to take form [12–14]; one where rovers and robots are not simple carriers, but actually constitute and support a modular, multi-expertize environment for complex planetary activities that can go from sample extraction, collection and processing, to the preparation of a base for manned exploration or resource gathering [13–21].

Despite the lack of an implementation in the real space environment, there is ongoing development on the subject of integrated robotic exploration; for example, Fink et al. [22] describe a framework for the robotic exploration of lava tubes of which there is strong evidence both on the Moon and on Mars.

Cordes et al., with the LUNARES project [24], describe the development of a framework for collaborative robotics with the intent of lunar craters exploration; static, wheeled, and legged robots are implemented.

Modular robotics applied to celestial bodies exploration has

E-mail addresses: stefano.seriani@phd.units.it (S. Seriani), pgallina@units.it (P. Gallina), armin.wedler@dlr.de (A. Wedler).
[1] Postal address: University of Trieste, Department of Engineering and Architecture, via A. Valerio 10, 34127, Trieste, Italy.

been also investigated by the RIMRES [24] and ROBEX [25] projects, which describes the collaborative operations of several heterogeneous autonomous robots. In particular, a wheeled rover with a serial manipulator is used to load, carry to target and deploy immovable modules on the ground that can contain scientific instrumentation, experiments or other devices like radio beacons.

A supervised autonomy tele-robotics experiment [26] under the METERON project demonstrated the use of the DLR's (Deutsches Zentrum für Luft und Raumfahrt) wheeled anthropomorphous robot Justin, for the maintenance of a solar array deployed in a space environment.

Cable Driven Parallel Robots (CDPRs) form a class of robots that exploit tethered mechanisms to manipulate the end-effector; in particular, the end-effector is suspended with cables and a coordinated system of winches handles the actuation, by varying the lengths of unwound cable. In general it is a well-known research subject, and extensive work has been performed over the years, as seen from [27–34]. An aspect which has seen comparatively low attention is that of sagging cables; the general trend is to approximate the tethers as negligible-mass components. Indeed, very few works have addressed sag by modeling cables as catenary curves [28,33,34].

With a few notable exceptions, CDPRs have seen poor implementation in the space environment; perhaps the best example is the NIST Robocrane, described by Roger et al. in 1993 [30].

Conversely, a topic which is very well developed in the space industry context is that of tethered systems, particularly orbital, as described in [35,36] or [32].

In this paper, we present a novel application of cooperative and modular robotics to the field of space exploration. This consists in a series of 3 modules that, when deployed, constitute a 3-links Cable Driven Parallel Robot (CDPR) that can perform efficiently tasks which require a large workspace and a lightweight structure. The modules themselves are arranged and deployed by a rover equipped with a serial manipulator with a docking interface instead of a conventional gripper.

In Section 2, the system is described in detail: the module, the end-effector and the deployment procedure are illustrated in depth. In Section 3 a complete pseudostatic model of the robot is presented; the stability of the modules is studied with the aid of the stability polytopes, and the groundwork for the characterization of the workspace is illustrated. In Section 4 the results of the analysis are reported and discussed, while in Section 5 a thorough analysis on possible applications is described.

2. Description of the system

The system consists of 3 types of components: the modules, the rover and the end-effector. Initially, these are separate and possibly stowed. The deployment process consists of positioning the 3 modules, and connecting the end-effector to the cables attached to each module; this procedure is carried out by the rover.

The CDPR, as mentioned in the introduction, consists in the 3 deployed modules, which provide the active winches that operate the cables. In the following subsections the module and the end-effector subsystems are presented. Finally, the deployment procedure is outlined, along with a general description of the rover.

2.1. The module

Each base module, as seen in Fig. 1, is a device which must be stable on rough terrain, provide structural integrity to the system, and perform its hardware control functions. In this work we focus on a module which is not fixed to the ground, but simply lies on top of it, relying on friction with the ground to keep its position.

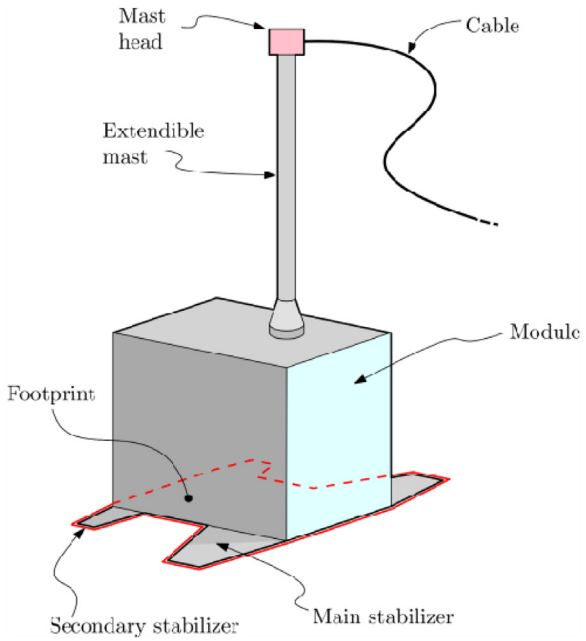

Fig. 1. A module of the 3-cable CDPR robot. The prism at the bottom contains the actuator for the extendible mast and the control system. The main and secondary stabilizers are illustrated at the very bottom, and the footprint is highlighted.

In order to coordinate the feed of the cables, a master-slaves configuration is advisable, where one module acts as the master, and the rest as its slaves; the master module provides all of the high-level functions, e.g. path-planning, vision, communication with the slaves, etc., whereas the slaves themselves will perform the lower-level functions, i.e. control of the winches, relative position control, etc.

Since the module is not fixed to the ground, a fundamental characteristic of it is its footprint, since it contributes to its stability when loads are applied by the cables. In this paper we discuss three different types; by looking at Fig. 1, one can see that two pairs of stabilizers exist, the “Main” and the “Secondary stabilizer”. These are lightweight deployable structures that widen the footprint of the module, thus making it less prone to tilting and ultimately toppling. We call “A” the situation where no stabilizer is present, “B” where only the main ones are deployed, and “C” where both the main and the secondary are open. It is worth noting that the stabilizers are placed only on the side of the module and not, for example, on the front; the rationale is that the module is comparably thin, so the stabilizers are placed to compensate the poor stability in the transversal direction.

The power-requirements of each modules are, for the purpose of this paper, based on the winches used for the cables. Considering a maximum speed of $0.5 ms^{-1}$, and a mass of 1Kg on the end-effector, this translates into approximately 5 W, relative to the worst possible load condition, in Earth gravity. Considering all possible losses, this figure could easily grow to 10/50 W.

2.2. The end-effector

The end-effector that we propose as an example in Fig. 2, consists of a body frame on which a pan-tilt camera is mounted. Since the component must be allowed to be disconnected from the cables, a docking system is employed for the connection. Since the cables should incorporate data and power transmission functions, the docking adapters must employ a coaxial connector.

In general, the only major limitation on the characteristics of end-effector is weight, as will become evident in the following

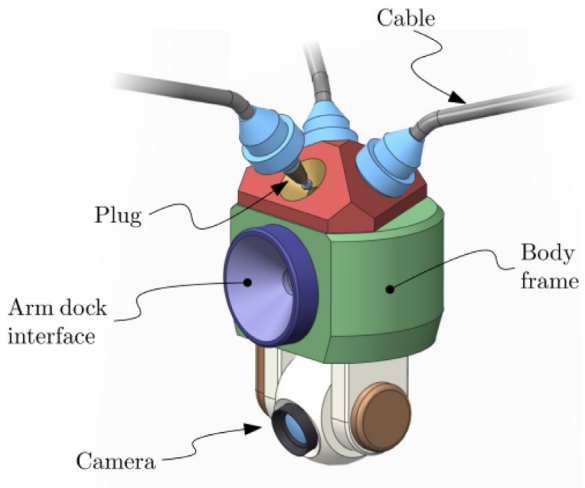

Fig. 2. The end-effector. The cables are connected through small lockable docking adapters which can host an electrical connector or plug.

sections. In Section 5, we discuss some possible alternatives. In order to determine the cables' characteristics, the power-consumption of the end-effector is estimated in approximately 100 W at full draw.

2.3. The cables

The cables are a central asset for the modular CDPR. Although the aim of this paper is not to provide a detailed design for the system, some technical insight might be useful to correctly frame this work. Given the power requirements of the end-effector, and considering a 48V line for the supply, the cable's linear mass can be assumed at 0.016Kg/m, for an AWG 17 cable, with a voltage drop of only 3.5% over 10 m. Regarding the structural strength, we chose an aramidic fiber braid (e.g. Kevlar). Since the projected maximum tension of the cables is in the order of 50N, this brings to a minimum diameter of a mere 0.1mm, and a linear mass of $4.72E-5$Kg/m. This can be considered negligible compared to the power-supply cables.

2.4. Deployment procedure

The deployment procedure consists mainly in two steps:

1. Positioning and setup of the 3 modules.
2. Connection of the end-effector to the cables' endpoints.

By referring to Fig. 3a one can appreciate how the modules can be carried around by the rover; a docking adapter is used in place of a conventional gripper, increasing robustness in the whole process. The same concept is used to manipulate the end-effector depicted in Fig. 2, which carries a docking adapter as well.

In order to fully describe the various phases of deployment, along with some possible paths of the rover, a schema is shown in Fig. 3b. In the figure, the area to cover is shown, along with the desired positions of the modules P_1', P_2' and P_3', around it.

To position the modules, the rover has to drive through path $t_a \rightarrow t_b \rightarrow t_c$, incrementally. At this point the modules' stabilizers deploy.

The placement of the end-effector is substantially more complex since it involves connecting and driving a tethered component; the procedure is as follows:

1. The rover picks up the end-effector from storage, by docking it to the arm.
2. It follows path segment t_d.
3. In P_1', the rover maneuvers the end-effector to connect to the cable of module 1 through the plug visible in Fig. 2.
   At this point, the rover is effectively tethered to module 1, and the path planner must account for any constraints posed by such connection.
4. The rover drives through segment t_e.
5. In proximity of P_2' it connects the cable of module 2 to the end-effector.
   The rover is now tethered to both module 1 and 2. This effectively means that the path planner must coordinate the feed of the cable of the two modules to follow the end-effector, which is moving along with the rover.
6. The rover drives through segment t_f.
7. At P_3', it connects the end-effector to the last cable.
8. The rover undocks the end-effector.
9. The masts of the modules extend.

The CDPR is now in place and the rover can be released.

3. Model of the CDPR

The CDPR is the heart of the integrated system. In order to analyze feasibility and performance, in the following sections, a full analytical model is given, along with the tools to evaluate it.

For the computations regarding the pseudostatics and the workspace analysis, the model for the cables is approximated as a straight line with negligible mass and zero deformation. This enhances computability at the cost of some accuracy. In order to determine the loss related to the sagging, we present as well a catenary-based model for the cables and we compare its results

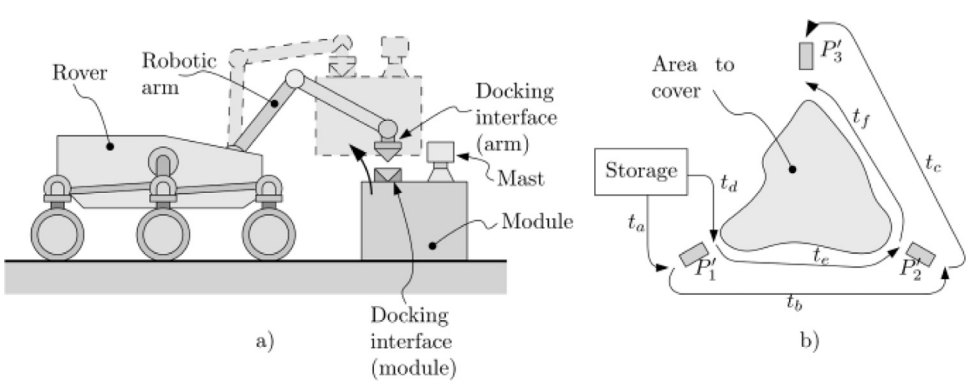

Fig. 3. Deployment procedure. In (a) the interaction of the rover with the module is shown. The docking interface on the arm side locks itself in the counterpart on the module and allows the module to be lifted and driven in place. In (b) the possible paths of the rover are shown as $\boldsymbol{t_a}$ through $\boldsymbol{t_f}$.

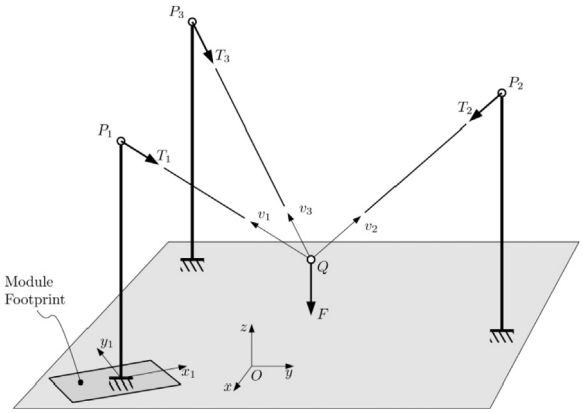

Fig. 4. Illustration of the pseudostatics scheme of the modular CDPR. The end-effector Q is suspended by the three cables of unit vectors $\boldsymbol{v}_{1,2,3}$, with tensions $\boldsymbol{T}_{1,2,3}$ to the cable feed mechanisms located in $\boldsymbol{P}_{1,2,3}$. The force $\boldsymbol{F}$ caused by gravity is applied to $\boldsymbol{Q}$. The module footprints are referred to the modules local coordinate systems ($\boldsymbol{x}_1$, $\boldsymbol{y}_1$, $\boldsymbol{z}_1$), ($\boldsymbol{x}_2$, $\boldsymbol{y}_2$, $\boldsymbol{z}_2$) and ($\boldsymbol{x}_3$, $\boldsymbol{y}_3$, $\boldsymbol{z}_3$), the last two of which are not shown.

with the ones given by the straight-line approximation. Along the same line, we illustrate a model for the deformation of the cable under tension.

3.1. Pseudostatics

The Pseudostatics of the CDPR is illustrated in Fig. 4 and consists of cables with negligible mass. The system is defined by the following governing vector equation,

$$\boldsymbol{F}+T_1\hat{\boldsymbol{v}}_1+T_2\hat{\boldsymbol{v}}_2+T_3\hat{\boldsymbol{v}}_3=0, \tag{1}$$

where $\hat{\boldsymbol{v}}_i$ is the unit vector of the i-th cable, defined as $\hat{\boldsymbol{v}}_i=(P_i-Q)/\|P_i-Q\|$.

Assumed the force $\boldsymbol{F}$ on the end-effector $\boldsymbol{Q}$ is known, in order to calculate the cable tensions $T_{1,2,3}$, these terms must be rendered explicit. Eq. (1) can be manipulated into this form,

$$\begin{bmatrix} v_{1,x} & v_{2,x} & v_{3,x} \\ v_{1,y} & v_{2,y} & v_{3,y} \\ v_{1,z} & v_{2,z} & v_{3,z} \end{bmatrix} \begin{Bmatrix} T_1 \\ T_2 \\ T_3 \end{Bmatrix} = \begin{Bmatrix} F_x \\ F_y \\ F_z \end{Bmatrix}, \tag{2}$$

Which is of the $Ax = b$ type, meaning it can be easily inverted as $x = A^{-1}b$; hence,

$$\begin{Bmatrix} T_1 \\ T_2 \\ T_3 \end{Bmatrix} = \begin{bmatrix} v_{1,x} & v_{2,x} & v_{3,x} \\ v_{1,y} & v_{2,y} & v_{3,y} \\ v_{1,z} & v_{2,z} & v_{3,z} \end{bmatrix}^{-1} \begin{Bmatrix} F_x \\ F_y \\ F_z \end{Bmatrix}. \tag{3}$$

The layout of the modules is illustrated in Fig. 5. We can, at this point, define the cable's tensions vectors, as $\boldsymbol{T}_i = -T_i\hat{\boldsymbol{v}}_i$, for the i-th module. These are applied to the cable's feed mechanism on top of the mast of the module, that is to say, to point $\boldsymbol{P}_i$, and can cause the module to topple over if certain conditions are met. This will be discussed in depth in the next section.

3.2. Stability polytope analysis

The stability of a rigid body which is placed on the ground in a still condition, is subject to gravity and to a general external force $\mathcal{F}$, can be defined as the subset of $\mathcal{F}$ for which the body is in a stable condition, i.e. remains still indefinitely. The main factors that come into play are the footprint of the body, the center of mass $\boldsymbol{G}$ position, the mass m itself of the body, the point of application of $\mathcal{F}$ and its magnitude. We do not consider possible sliding of the module on the ground. These are illustrated in Fig. 6, where, notably, $\mathcal{F}$ coincides to $\boldsymbol{T}_i$ (i.e. the cable tension) and the

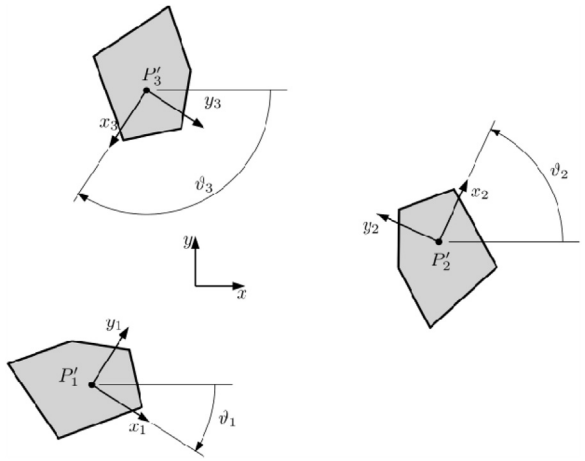

Fig. 5. View from the top of the footprints of the modules. The polygon representing the footprint is identical in the three cases, and is positioned in points $\boldsymbol{P}'_{1,2,3}$, with a rotation along the $\boldsymbol{y}_{1,2,3}$ axes of angles $\vartheta_{1,2,3}$ respectively. These rotations generate the local frame of references ($\boldsymbol{x}_1$, $\boldsymbol{y}_1$, $\boldsymbol{z}_1$), ($\boldsymbol{x}_2$, $\boldsymbol{y}_2$, $\boldsymbol{z}_2$) and ($\boldsymbol{x}_3$, $\boldsymbol{y}_3$, $\boldsymbol{z}_3$). Note that the shapes used for this representation are purely indicative.

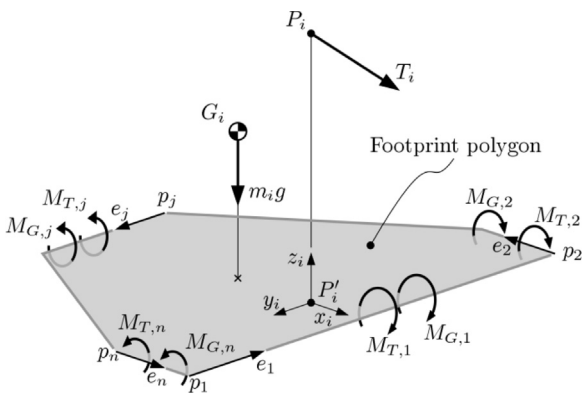

Fig. 6. Stability analysis quantities. For each module $\boldsymbol{i}$ the cable tension $\boldsymbol{T_i}$ is applied to $\boldsymbol{P_i}$ and generates momentums $\boldsymbol{M_{T,j}}$ around the footprint polygon $\boldsymbol{p}_{1,\ldots,n}$ sides unit vectors $\hat{\boldsymbol{e}}_{\boldsymbol{j}}$. The same applies to the force of gravity $\boldsymbol{m_ig}$, which, applied to the center of mass $\boldsymbol{G_i}$ generates $\boldsymbol{M_{G,j}}$.

footprint is defined by the polygon of vertices $\boldsymbol{p}_1,\ldots,\boldsymbol{p}_j,\ldots,\boldsymbol{p}_n$, where n is the number of sides of the polygon. Note that the footprint seen in Fig. 6 is the planar convex hull of the original footprint of the module found in Fig. 1; this is a general requirement of the method.

It is possible to calculate the momentum that $\boldsymbol{T_i}$ generates along the unit vectors $\hat{\boldsymbol{e}}_j$ which need to be defined in a counter-clockwise pattern, as seen in the figure. Let us call $\boldsymbol{r}_{T,j}$ the projection of $\boldsymbol{P}_i-\boldsymbol{p}_j$ on a plane for which $\hat{\boldsymbol{e}}_j$ is the normal (see Fig. 6); similarly, let $\boldsymbol{r}_{G,j}$ be the projection of $\boldsymbol{G}_i-\boldsymbol{p}_j$ on the same plane. Then we have,

$$\begin{cases} \boldsymbol{M}_{T,j} = \boldsymbol{r}_{T,j}\times\boldsymbol{T}_i \\ \boldsymbol{M}_{G,j} = \boldsymbol{r}_{G,j}\times m_i\boldsymbol{g} \end{cases}. \tag{4}$$

The condition for stability can be expressed as,

$$(\boldsymbol{M}_{T,j}+\boldsymbol{M}_{G,j})\bullet\boldsymbol{e}_j\leq 0,\ \forall j\in 1,\ \ldots,n. \tag{5}$$

As previously stated, the general requirement for which Eq. (5) – and the relative methodology – is applicable, is that the footprint must be a convex polygon.

In Fig. 7a possible polytope computation is visible for the three different footprint polygons A, B and C. In this case, the external force $\mathcal{F}$ is placed on a plane parallel to the ground. Where φ is the angle between the force vector and the y axis of the module, the

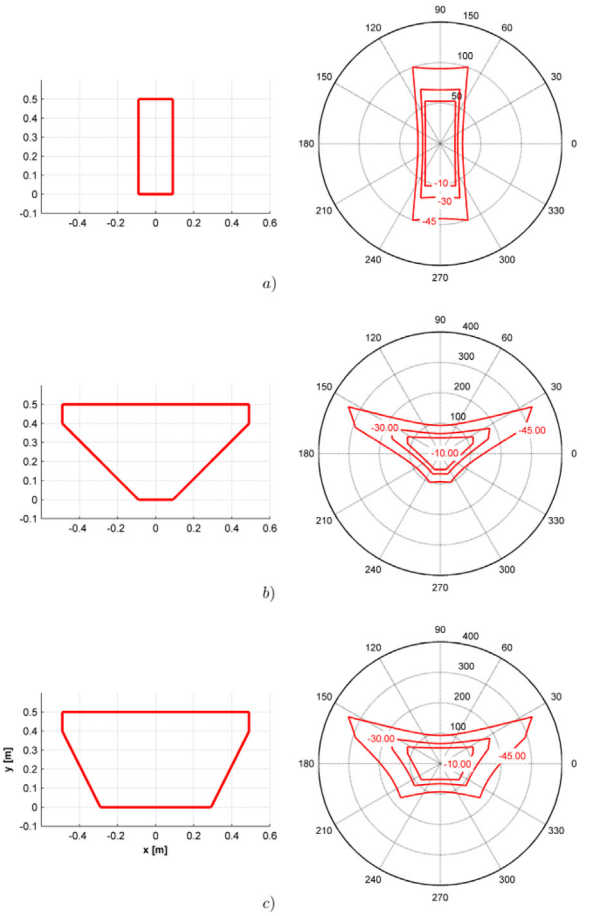

Fig. 7. Shape of the stability polytopes for different footprints $\boldsymbol{p}_{j,A}$, $\boldsymbol{p}_{j,B}$ and $\boldsymbol{p}_{j,C}$, which are visible respectively on the left, in (a), (b) and (c). For each footprint three different deflection angles from the horizontal plane are shown: −45°, −30° and −10°.

general point of the polytope is as follows,

$$\rho(\varphi)=\min\left(-\frac{\left(\boldsymbol{r}_{G,j}\times m\boldsymbol{g}_j\right)\bullet\boldsymbol{e}_j}{\left(\boldsymbol{r}_{T,j}\times\hat{\boldsymbol{T}}_i(\varphi)\right)\bullet\boldsymbol{e}_j}\right), \tag{6}$$

where $\hat{\boldsymbol{T}}_i(\varphi)=\boldsymbol{T}_i/\|\boldsymbol{T}_i\|$, and $j=1,\ldots,n$. In essence, ρ is the ratio between the stabilizing moment generated by the gravity vector, and the toppling moment caused by $\mathcal{F}$. The minimum function is used in order to locate the smallest ratio (i.e. the less stable one) amongst those generated by each of the n sides of the polygon. The values can then be normalized in the 0 – 1 interval, as follows,

$$\rho'(\varphi)=\rho/\max(\rho). \tag{7}$$

The $\rho'(\varphi)$ value represents the minimum normalized force, oriented along the direction given by φ, required to hinder the stability of the rigid body. Some collections of values of $\rho(\varphi)$, represented in polar form, are plotted in Fig. 7a through c, on the right. It is important to note that this ρ is dependent on other parameters, e.g. the center of mass G_i location, and the location of point P_i. They are not quantitatively taken in consideration in this example.

3.3. Workspace analysis of the CDPR

When viewed from above, the *reachable* workspace W_r of a 3-link CDPR subject to gravity has a triangular shape with the vertices coincident with the cable anchor points. This is a result of the following condition on the cables' tensions,

$$T_i\geq 0, \tag{8}$$

which applies to Eq. (3).

Within the reachable workspace, depending on the position of $\boldsymbol{Q}$, $\boldsymbol{P}_1$, $\boldsymbol{P}_2$ and $\boldsymbol{P}_3$, and the force $\boldsymbol{F}$, the values of T_i can change considerably. One can define a *manipulability* workspace W_m, where the stability of the modules is guaranteed for each point $\boldsymbol{Q}\in W_m$. As stated in Section 3.2, this is given when Eq. (5) holds.

It might be useful to define an index I_t to better evaluate the closeness to tilting; if we take into consideration the moments defined in Eq. (4), we can write the following,

$$I_t\left(\boldsymbol{Q},\boldsymbol{P}_i,\boldsymbol{F},m,\boldsymbol{p}_j\right)=\max\left(\boldsymbol{M}_{T,j}/\boldsymbol{M}_{G,j}\right), \tag{9}$$

where j represents, as usual, the j-th side of the footprint polygon $\boldsymbol{p}_j$, i the i-th module and m the mass of the module. The maximum function is used in order to locate the highest ratio amongst those generated around the n sides of the polygon.

The tilt index I_t is defined in the $[0,+\infty]$ interval, hence the following holds,

$$\begin{cases} I_t\in[0,1] & \textit{Stability} \\ I_t\in[1,+\infty] & \textit{Instability} \end{cases}. \tag{10}$$

3.4. Catenary-based model

The general planar parametric equation for a catenary curve of linear mass ρ, subject to a gravity acceleration of module g, can be written [37] as,

$$\xi'=\frac{H}{\rho g}\left(\cosh\left(\frac{\rho\zeta'}{H}\right)-1\right), \tag{11}$$

where, as shown in Fig. 8, H is the horizontal constraint reaction on the supports and is constant along the entire assembly. It is useful to determine a "virtual" coordinate system (ξ',ζ'), which also mirrors (ξ,ζ). In order to couple the mass m_E, an artifice can be used where the mass of the dash-dotted segment $\widehat{B\Omega}$ of the catenary is defined as equal to m_E. Hence, this follows,

$$B_{\zeta'}=\frac{H}{\rho g}\operatorname{asinh}\left(\frac{m_E g}{H}\right). \tag{12}$$

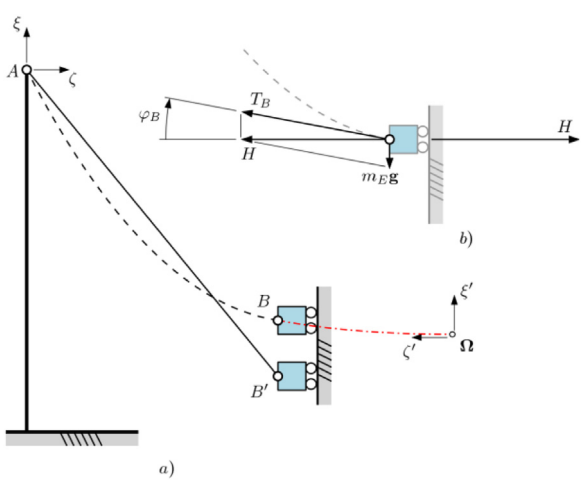

Fig. 8. Catenary-based model for the cables of the CDPR. In (a), the general definitions are given, considering the end-effector as a mass $\boldsymbol{m_E}$ suspended by cable $\boldsymbol{AB}$. The straight-line model is shown as comparison ($\bar{\boldsymbol{AB}}'$). The cylindrical symmetry of the three-cable system is represented by the vertical linear constraint on point $\boldsymbol{B}$ and $\boldsymbol{B}'$. In (b) the forces acting on $\boldsymbol{B}'$ are shown.

Furthermore, $A_{\zeta'}$ can be computed, since, in this instance, the distance $\overline{AB}$ projected on ζ is a starting parameter. The remaining coordinates of points A and B are determined as follows,

$$\begin{aligned} B_{\xi'} &= \frac{H}{\rho g}\cosh\left(\operatorname{asinh}\frac{m_E g}{H}\right)-1 \\ A_{\xi'} &= \cosh\frac{A_{\zeta'}\rho g}{H}-1 \end{aligned}, \tag{13}$$

Finally, the coordinates can be transformed as $(\xi', \zeta')\longrightarrow(\xi, \zeta)$. It is important to note that the model is not explicit (see Eqs. (11)–(13)), and requires a certain amount of numerical computation.

Ultimately, this formulation allows to compute the error between the models, which consists in the distance ε_y, as follows,

$$\varepsilon_{y,s}=\varepsilon_{\xi}=\varepsilon_{\xi'}=\|B-B'\|. \tag{14}$$

3.5. Deformable cable model

Given that the length of the cables can reach large values, we show how this effect can impact accuracy. Leaning on elasticity theory, we see that the elongation of a cable is $\Delta L_i=T_i L_{i,0}/\tau$, where $L_{i,0}=\|Q-P_i\|$, and $\tau = E_k S_k+E_{cu}S_{cu}$, with E_k and E_{cu} being Young's modulus of Kevlar and copper respectively. S_k and S_{cu} are the cross-sectional areas for the two components. Finally, using the straight-line model, one can compute the error,

$$\varepsilon_{y,d}=\sqrt{\left(L_{i,0}+\Delta L_i\right)^2-\|Q-P_i\|_x^2}-\sqrt{L_{i,0}{}^2-\|Q-P_i\|_x^2}\,. \tag{15}$$

4. Results and discussion

Since I_t is, in general, a very high dimension hypersurface, a completely coupled analysis would be impractical, impossible to visualize and computationally too expensive. It is though convenient to slice I_t along some of the most interesting dimensions, namely the configuration of angles ϑ_1, ϑ_2 and ϑ_3. Let us define a general angle ϑ^*. In order to simplify the partitioning, we assign the following constraints,

$$\begin{aligned} \vartheta_1&=\vartheta^* \\ \vartheta_2&=\vartheta^*-\pi/3 \\ \vartheta_3&=\vartheta^*-2\pi/3+\vartheta_3 \end{aligned}. \tag{16}$$

The other parameters are fixed and their values are summarized in Table 1.

By means of Eqs. (3), (4) and (9), it is possible to define the values of $I_t(\boldsymbol{Q},\vartheta^*)$ for every $\boldsymbol{Q}\in W_m$; if $\boldsymbol{Q}$ is selected always at the same height from the ground, this produces a set of surfaces $\boldsymbol{S}(\vartheta^*)=\bigcup I_t(\boldsymbol{Q},\vartheta^*),\forall\boldsymbol{Q}\in W_m$, one for each value of ϑ^*. It is then possible to discretize $\vartheta^*=0, \ldots, 2\pi$, in order to analyze the impact the angle ϑ^* has on the workspace morphology and index. For example, we can define the following quantity,

$$I_{t,max}\left(\vartheta^*\right)=\max\left(\boldsymbol{S}\left(\vartheta^*\right)\right), \tag{17}$$

which can be determined for each and every ϑ^*. The values are plotted in Fig. 9 for the three footprint configurations A, B and C, visible in Fig. 7 and defined in Table 1.

By looking at the curves, it is immediately apparent how configuration A is the least stable, with the majority of angular positions ϑ^* resulting in tilting or toppling ($I_t>1$) for the parameters used in this setup. Configurations B and C show, instead, good stability for every angular position, while the global minima of I_t is reached by configuration C at $\vartheta^*_{best}\cong 0.6\pi$, with $I_t(\vartheta^*_{best})\cong 0.3$.

A map of the workspace defined by the stability index I_t is visible in Fig. 10; it is relative to the height of $\boldsymbol{Q}_z=0$ and shows the stability configuration along the entire working area. The deep-blue area outside the central triangle is considered forbidden because the system would not be stable. In fact, should the end-effector lay there, a situation in which at least one of the cable tensions T_i would be negative. Since this cannot happen because of the structural nature of the cables, that location cannot be – at least statically – reached.

Quantitatively, at this height the robot is very stable, with a maximum value of $I_{t,max}=0.31$; in fact, approximately 77% of the area in the central triangle pertain to the interval between $I_t=0.2$ and $I_t=0.3$. In Fig. 11 it can be seen how the stability and workspace morphology changes in response to different heights of the end-effector $\boldsymbol{Q}$. In particular, in the last row of the grid, it is clear that the workspace *erodes* very fast, approaching the 2.5m level. This is due to the structural and geometrical characteristics of the CDPR; sure enough, the cables' tensions rapidly grow to a level where the momentums generated on the modules are so high that stability is compromised in at least one module.

Up until now we have considered cables with negligible mass. Conversely, Fig. 12 shows the results of the comparison between the catenary- and straight-line based models. This particular configuration corresponds to the one where the end-effector is in the center of the triangular workspace shown in Fig. 11 Fig. 10. A certain amount of sag in the cable exists, which causes a raise in the height of the end-effector. Given the value ρ given in Section 2.3, the geometry shown in Fig. 10 and a height of 3m from the end-effector to the top of the mast, a discrepancy $\epsilon_{y,c}=0.081$m or, relatively to the width of the workspace, $\varepsilon_{y,c,\%}=0.8\%$.

It can be shown that, for the same conditions, the error between the straight-line and the deformable-cable models is $\epsilon_{y,d}=0.009$m, or $\varepsilon_{y,d,\%}=0.08\%$ relative to the width of the workspace.

We find that the small size of the relative errors fully justifies the approximate straight-line model highlighted in Section 3.1.

Table 1
Fixed parameters for the CDPR robot. Note that the value $\boldsymbol{Q}_z$ denotes the height in the z-direction at which the workspace is computed. Gravity is assumed equal to g=9.81ms^{-2}.

Parameter	Value	Unit
m_{module}	20	Kg
$m_{end-eff}$	1	
$\boldsymbol{F}$	[0 0 −9.81]	N
$\boldsymbol{Q}_z$	0	m
$\boldsymbol{P}_i$	$\boldsymbol{P}_1$= [0 0 3]	
	$\boldsymbol{P}_2$= [5 10 cos(π/6) 3]	
	$\boldsymbol{P}_3$= [−5 10 cos(π/6) 3]	
$\boldsymbol{p}_j\,\vert_A$	$\boldsymbol{p}_1$= [−0.09 0.5 0]	
	$\boldsymbol{p}_2$= [0.09 0.5 0]	
	$\boldsymbol{p}_3$= [0.09 0 0]	
	$\boldsymbol{p}_4$= [−0.09 0 0]	
$\boldsymbol{p}_j\,\vert_B$	$\boldsymbol{p}_1$= [−0.49 0.5 0]	
	$\boldsymbol{p}_2$= [0.49 0.5 0]	
	$\boldsymbol{p}_3$= [0.49 0.4 0]	
	$\boldsymbol{p}_4$= [0.09 0 0]	
	$\boldsymbol{p}_5$= [−0.09 0 0]	
	$\boldsymbol{p}_6$= [−0.49 0.4 0]	
	$\boldsymbol{p}_7$= [−0.49 0.5 0]	
$\boldsymbol{p}_j\,\vert_C$	$\boldsymbol{p}_1$= [−0.49 0.5 0]	
	$\boldsymbol{p}_2$= [0.49 0.5 0]	
	$\boldsymbol{p}_3$= [0.49 0.4 0]	
	$\boldsymbol{p}_4$= [0.29 0 0]	
	$\boldsymbol{p}_5$= [−0.29 0 0]	
	$\boldsymbol{p}_6$= [−0.49 0.4 0]	
	$\boldsymbol{p}_7$= [−0.49 0.5 0]	

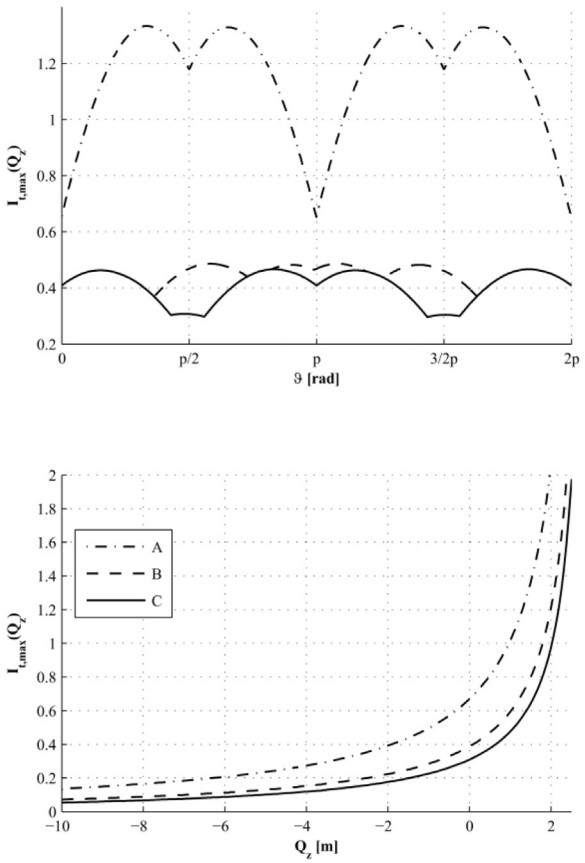

Fig. 9. Characterization of the tilting index. The top plot shows the relation between the angle ϑ of the modules and the tilting index $I_{t,max}$ for the different footprints. The discretization steps are $\delta\vartheta=2\pi/1000$ and $\delta x=\delta y\cong 0.47$m. The bottom plot shows $I_{t,max}(Q_z)$. Discretization is $\delta x\cong 0.17$m, $\delta y\cong 0.15$m and $\delta Q_z\cong 0.06$m.

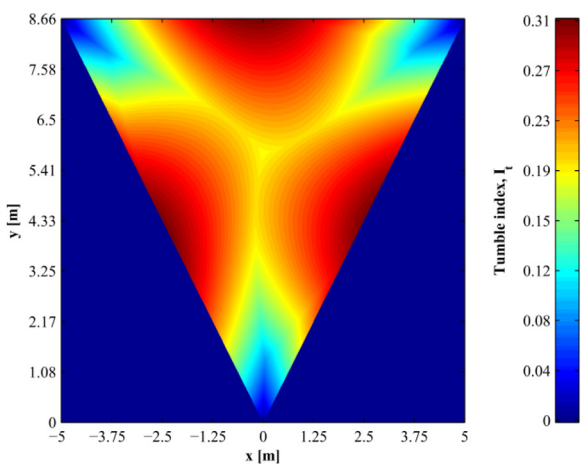

Fig. 10. Map of the workspace of the modular CDPR at ground level. The angular position of the modules is $\vartheta^*=1.384\pi$. Spatial discretization of the domain is, in this case, $\delta x=\delta y=0.01$m. (For interpretation of the references to color in this figure, the reader is referred to the web version of this article.)

Moreover, the two errors act in the opposite directions, with the cables' sagging contributing to a general increase in the height of the end-effector, and the deformation of the cables to a comparable decrease.

Finally, one should consider that, while the cables indeed add mass to the suspended portion of the robot, the tension acting on the top of the masts tends to be directed downwards by both the sag of the cable and its deformation. This has a positive effect on the stability of the modules.

5. Applications

As mentioned in the introduction, if complex structures or arrays of constructs are deployed on the surface of celestial bodies like Mars or the Moon, steps must be taken towards making maintenance and inspection of these systems possible and efficient. Automating these tasks is of paramount importance even in case of a manned presence, since extravehicular activities are generally to be avoided wherever possible.

Let us consider a possible solar panel array. Since size is, in this case, directly proportional to energy production, the ground area should conceivably be very large. The modular CDPR presented in this work could provide an affordable and efficient mean to inspect this structure, as illustrated in Fig. 13. Furthermore, as the last two decades of exploration on Mars with Pathfinder, MER-A, MER-B and MSL rovers from NASA demonstrate [38–40], dust deposition over time is a major problem. To mitigate this, the modular CDPR, equipped with a simple wiping device, could be used for the removal of the dust.

Regarding this particular application, the DLR tackled the problem with an approach [26] based on a wheeled anthropomorphous robot called Justin which could perform both the inspection and maintenance of the system. However, this procedure is very complex in relation to the task to be carried out, especially regarding inspection activities. Perhaps a joint approach would be more efficient, where the modular CDPR acts as the inspection device, and the wheeled robot as the manipulation and maintenance system. This would limit very much the overall complex activity of the latter, increasing the global efficiency.

A very promising concept for a possible base on Mars or the Moon is inflatable structures [17–19]; one major issue for these is the structural integrity of the shell. Frequent inspections by rover or other conventional device (or even manned) would be hard, especially on the top portions of the dome. The modular CDPR could be deployed around the dome and provide fast inspection capabilities to the most inaccessible parts of the structure.

Celestial body ground geological surveys seek a collection of samples from large extensions of the surface to provide a representative set. This, in turn, requires a close-up investigation of potential sampling locations [21], which can be very inefficient and time-consuming with a conventional rover. A modular CDPR could allow a first inspection of a large surface (e.g. around 100m^2 referring to Table 1) with relative ease. Furthermore, since the modules can be moved by the rover even when the robot is assembled, a simultaneous collaborative approach can be envisioned: the rover collects samples on the area previously surveyed by the CDPR, while, in the meantime, the CDPR surveys a neighboring area. The iteration of this process can, in principle, allow covering very large planetary surfaces.

Along the same lines, the CDPR could be exploited for the exploration of lava tubes [22], as visible in Fig. 14, either through simple visual inspection or as a deployment system for small rovers. Furthermore, some craters show very steep walls, which pose the same challenges [23] to exploration. In fact, in Fig. 9 one can see that a configuration where the load is lower than the ground level (such as is the case of any depression) has a very low tilting index $I_{t,max}$, which would increase stability of the modules and the overall payload capacity.

As a last application example, the modular CDPR could be used as an efficient means of transport between the modules of a robotic or manned base, without the need to erect complex and unreconfigurable structures.

6. Conclusion

In this paper, a complex deployable and reconfigurable

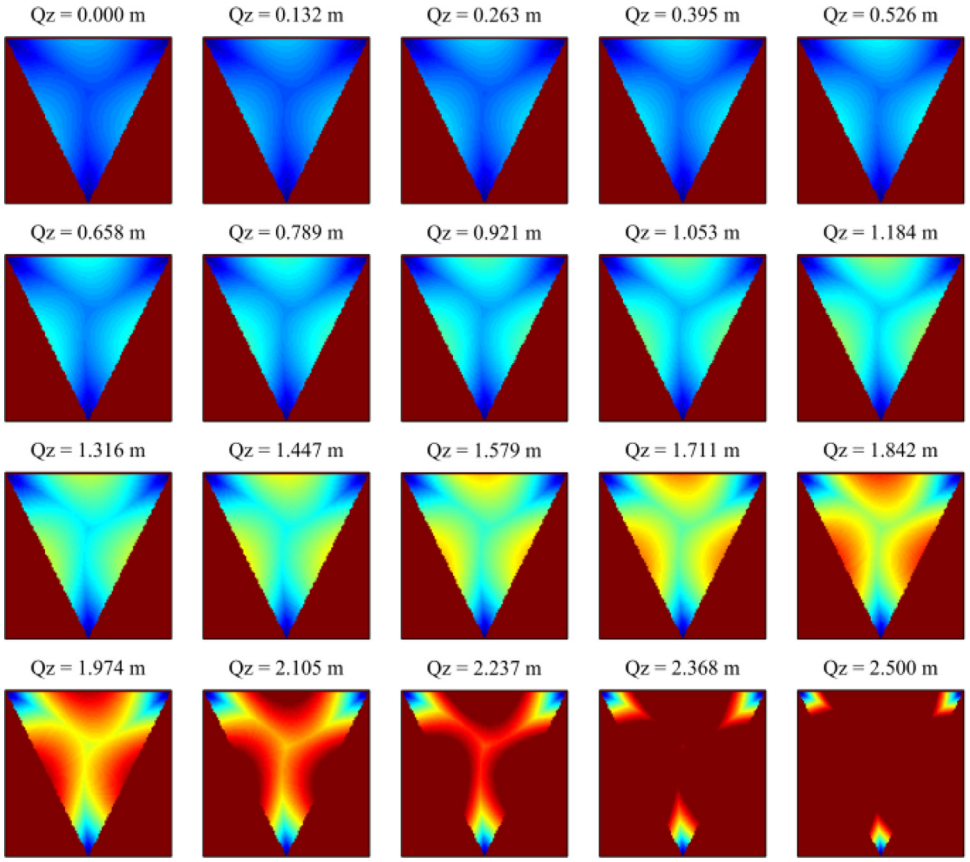

Fig. 11. Mosaic of the configurations of the workspace at varying heights from the ground. Note that the color red represents $I_t \geq 1$ (instability) – and is in fact used as a threshold – while blue stands for $I_t = 0$ (stability). (For interpretation of the references to color in this figure legend, the reader is referred to the web version of this article.)

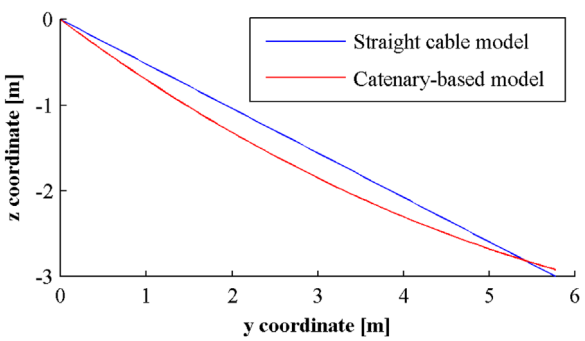

Fig. 12. Comparisons between the catenary-based and the straight cable model. The coordinates are relative to the workspace map in Fig. 10.

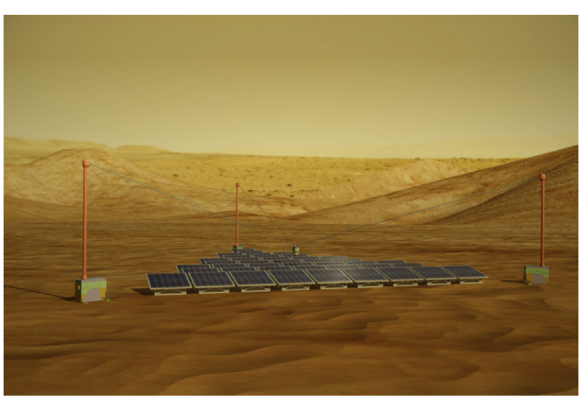

Fig. 13. Application of the modular CDPR for the maintenance of a large ground-deployed solar array.

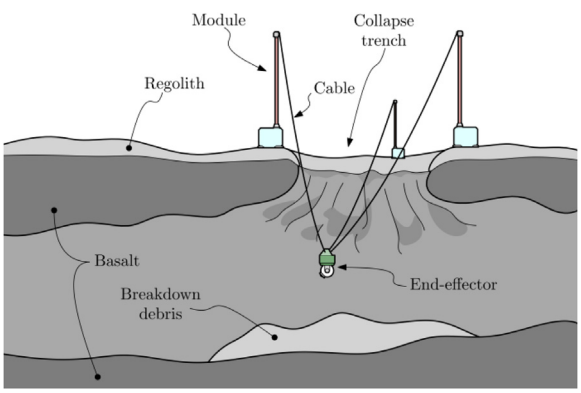

Fig. 14. Application of the modular CDPR to the exploration of lava tubes on celestial bodies. The end-effector shown is in the form of a pan-tilt camera system.

modular CDPR was designed for space exploration on celestial bodies. The architecture is composed of three standalone modules, an end-effector, and a rover with a robotic manipulator. In Section 1, literature on the broad subject of rovers for space applications is reported, as well as on the subject of modular robotics and cable robots in the same field. In Section 2, the deployment procedure is illustrated in detail, and the main sub-systems were described in depth. A complete model of the CDPR was presented in Section 3, taking advantage, among others, of the stability polytopes of the modules; this was used to perform a preliminary workspace analysis and to show the main design parameters, as illustrated in Section 4. Possible applications are discussed in Section 5, specifically in the field of visual inspection and light manipulation. For example, a setup for inspecting a large solar panel array (in the

order of 100m^2) is described; furthermore, the system is exploitable to investigate lava tubes and possibly as a deployment device for smaller rovers in these natural structures.

In accordance with the review of literature, our work indicates that modular or hybrid robotics shows increasing potential in tackling the challenges posed by space exploration in a context of long-term presence.

Acknowledgments

This work was supported in part by the Helmholtz Association, project alliance ROBEX, under contract number HA-304.

References

[1] D.R. Woods, Review of the soviet lunar exploration programme, Spaceflight 18 (7–8) (1976) 273–290.
[2] A.M.M. Teles, Mars astrobiology: recent status and progress, Planet. Explor. Sci.: Recent Results Adv. (2015) 147–245.
[3] H.P. Klein, The viking biological investigations: review and status, Orig. Life 9 (2) (1978) 157–160.
[4] K.C. Clausen, H. Hassan, M. Verdant, P. Couzin, G. Huttin, M. Brisson, C. Sollazzo, J.-P. Lebreton, The Huygens Probe system design, Space Sci. Rev. 104 (1–4) (2002) 155–189.
[5] J. Biele, S. Ulamec, B. Feuerbacher, H. Rosenbauer, R. Mugnuolo, D. Moura, J. P. Bibring, Current status and scientific capabilities of the Rosetta Lander payload, Adv. Space Res. 29 (8) (2002) 1199–1208.
[6] J.P. Grotzinger, J. Crisp, A.R. Vasavada, R.C. Anderson, C.J. Baker, R. Barry, D. F. Blake, P. Conrad, K.S. Edgett, B. Ferdowski, R. Gellert, J.B. Gilbert, M. Golombek, J. Gómez-Elvira, D.M. Hassler, L. Jandura, M. Litvak, P. Mahaffy, J. Maki, M. Meyer, M.C. Malin, I. Mitrofanov, J.J. Simmonds, D. Vaniman, R. V. Welch, R.C. Wiens, Mars Science Laboratory mission and science investigation, Space Sci. Rev. 170 (1–4) (2012) 5–56.
[7] J.N. Goswami, M. Annadurai, Chandrayaan-2 Mission, in: Proceedings of the 42nd Lunar and Planetary Science Conference, held March 7–11, 2011 at the Woodlands, Texas. LPI Contribution No. 1608, p. 2042.
[8] J. Vago, B. Gardini, G. Kminek, P. Baglioni, G. Gianfiglio, A. Santovincenzo, S. Bayón, M. Van Winnendael, ExoMars: searching for life on the red planet, Eur. Space Agency Bull. 126 (2006) 16–23.
[9] J.F. Mustard, M. Adler, A. Allwood, D.S. Bass, D.W. Beaty, J.F. Bell III, W.B. Brinckerhoff, M. Carr, D.J. Des Marais, B. Drake, K.S. Edgett, J. Eigenbrode, L.T. Elkins-Tanton, J.A. Grant, S.M. Milkovich, D. Ming, C. Moore, S. Murchie, T.C. Onstott, S.W. Ruff, M.A. Sephton, A. Steele, A. Treiman, Appendix to the Report of the Mars 2020 Science Definition Team, posted July, 2013, by the Mars Exploration Program Analysis Group (MEPAG), 2013, 51pp. At: ⟨http://mepag.jpl.nasa.gov/reports/MEP/Mars_2020_SDT_Report_Appendix.pdf⟩.
[10] M.P. Golombek, R.A. Cook, T. Economou, W.M. Folkner, A.F.C. Haldemann, P. H. Kallemeyn, J.M. Knudsen, R.M. Manning, H.J. Moore, T.J. Parker, R. Rieder, J. T. Schofield, P.H. Smith, R.M. Vaughan, Overview of the Mars Pathfinder Mission and assessment of landing site predictions, Science 278 (5344) (1997) 1743–1748.
[11] W.-H. Ip, J. Yan, C.-L. Li, Z.-Y. Ouyang, Preface: ehe chang'e-3 lander and rover mission to the Moon, Res. Astron. Astrophys. 14 (12) (2014) 1511–1513.
[12] A. Scott Howe, K.J. Kennedy, T. Gill, NASA Habitat Demonstration Unit (HDU) Deep Space Habitat analog, in: Proceedings of AIAA SPACE 2013 Conference and Exposition, 2013.
[13] A. Muscatello, E. Santiago-Maldonado, Mars in situ resource utilization technology evaluation, in: Proceedings of the 50th AIAA Aerospace Sciences Meeting Including the New Horizons Forum and Aerospace Exposition. January 2012.
[14] A. Wedler, M. Hellerer, B. Rebele, H. Gmeiner, B. Vodermayer, T. Bellmann, S. Barthelmes, R. Rosta, C. Lange, L. Witte, N. Schmitz, M. Knapmeyer, A. Czeluschke, L. Thomsen, C. Waldmann, S. Flogel, M. Wilde, Y. Takei, ROBEX – components and methods for the planetary exploration demonstration, in: Proceedings of the 13th Symposium on Advanced Space Technologies in Robotics and Automation (ASTRA), May 2015.
[15] B. Kading, J. Straub, Utilizing in-situ resources and 3D printing structures for a manned Mars mission, Acta Astronaut. 107 (2015) 317–326.
[16] O. Barbera, F. Mailland, S. Hovland, G. Giacoppo, Energy and provision management study: a research activity on fuel cell design and breadboarding for lunar surface applications supported by European Space Agency, Int. J. Hydrog. Energy 39 (26) (2014) 14079–14096.
[17] L. Levrino, G. Gatto, S. Hall, J. Wellons, E. Gargioli, J.A. Hoffman, P. Maggiore, N. Viola, M.A. Viscio, Human life support in permanent lunar base architectures, in: Proceedings of the International Astronautical Congress, IAC, 13, 2014, pp. 9690–9700.
[18] Y. Tu, Multi-spherical-surface geometric configurations and analyses of inflatable combined cable-membrane structure for lunar habitation, Adv. Space Res. (2015).
[19] S.S. Schreiner, T.P. Setterfield, D.R. Roberson, B. Putbrese, K. Kotowick, M. D. Vanegas, M. Curry, L.M. Geiger, D. Barmore, J.J. Foley, P.A. Latour, J. A. Hoffman, J.W. Head, An overnight habitat for expanding lunar surface exploration, Acta Astronaut. 112 (2015) 158–165.
[20] I.A. Crawford, Lunar resources: a review, Prog. Phys. Geogr. 39 (2) (2015) 137–167.
[21] L.E. Borg, D.J. Des Marais, D.W. Beaty, O. Aharonson, S.A. Benner, D.D. Bogard, J. C. Bridges, C.J. Budney, W.N. Calvin, B.C. Clark, J.L. Eigenbrode, M.M. Grady, J. W. Head, S.R. Hemming, N.W. Hinners, V. Hipkin, G.J. MacPherson, L. Marinangeli, S.M. McLennan, H.Y. McSween, J.E. Moersch, K.H. Nealson, L. M. Pratt, K. Righter, S.W. Ruff, C.K. Shearer, A. Steele, D.Y. Sumner, S.J. Symes, J. L. Vago, F. Westall, Science priorities for Mars sample return, Astrobiology 8 (3) (2008) 489–535.
[22] W. Fink, V.R. Baker, D. Schulze-Makuch, C.W. Hamilton, M.A. Tarbell, Autonomous exploration of planetary lava tubes using a multi-rover framework, in: Proceedings of IEEE Aerospace Conference, 2015 June, art. no. 7119315, 2015.
[23] F. Cordes, I. Ahrns, S. Bartsch, T. Birnschein, A. Dettmann, S. Estable, S. Haase, J. Hilljegerdes, D. Koebel, S. Planthaber, T.M. Roehr, M. Scheper, F. Kirchner, LUNARES: Lunar crater exploration with heterogeneous multi robot systems, Intell. Serv. Robot. 4 (1) (2011) 61–89.
[24] F. Cordes, F. Kirchner, Reconfigurable integrated multirobot exploration system (RIMRES): heterogeneous modular reconfigurable robots for space exploration, J. Field Robot. 31 (1) (2014) 3–34.
[25] D. Leidner, A. Wedler, S. Music, Robotic deployment of extraterrestrial seismic networks, in: Proceedings of the 13th Symposium on Advanced Space Technologies in Robotics and Automation (ASTRA), 2015.
[26] N.Y. Lii, D. Leidner, A. Schiele, P. Birkenkampf, R. Bayer, B. Pleintinger, A. Meissner, A. Balzer, Simulating an extraterrestrial environment for robotic space exploration: the METERON supvis-Justin telerobotic experiment and the solex proving ground, in: Proceedings of the 13th Symposium on Advanced Space Technologies in Robotics and Automation (ASTRA), at ESA/ESTEC, Noordwijk, The Netherlands. 2015 May.
[27] J. Lamaury, M. Gouttefarde, M. Michelin, O. Tempier, Design and Control of a Redundant Suspended Cable-Driven Parallel Robots: Latest Advances in Robot Kinematics, Springer, Netherlands, 2012, pp. 237–244.
[28] J.-P. Merlet, On the inverse kinematics of cable-driven parallel robots with up to 6 sagging cables, in: Proceedings of IEEE International Conference on Intelligent Robots and Systems, 2015 December, Art. no. 7353995, 2015, pp. 4356–4361.
[29] J. Albus, R. Bostelman, N. Dagalakis, The NIST robocrane, J. Robot. Syst. 10 (1993) 709–724.
[30] Roger Bostelman, James Albus, Karl Murphy, Tsung-Ming Tsai, Amatucci, (Eds.), A Stewart Platform Lunar Rover, in: Proceedings of the Space '94 Conference, Albuquerque, NM, 1994.
[31] P.D. Campbell, P.L. Swaim, C.J. Thompson, Charlotte™ robot technology for space and terrestrial applications, Training 2014 (1996) 05–07.
[32] A. Wedler, M. Chalon, A. Baumann, W. Bertleff, A. Beyer, J.B. Robert Burger, M. Grebenstein, R. Gruber, F. Hacker, E. Kraemer, K. Landzettel, M. Maier, H.-J. Sedlmayr, N. Seitz, F. Wappler, B. Willberg, T. Wimboeck, F. Didot, and G. Hirzinger, DLR's space qualifiable multi-fingered dexhand, in: Proceedings of the 11th Symposium on Advanced Space Technologies in Robotics and Automation (ASTRA), ESA/ESTEC, Noordwijk, the Netherlands, vol. 11, p. Session 3a, ESA, ESA, 12–14 April 2011.
[33] M. Gouttefarde, et al., Simplified static analysis of large-dimension parallel cable-driven robots, in: Proceedings of IEEE International Conference on Robotics and Automation, Saint Paul, May, 14–18, 2012, pp. 2299–2305.
[34] D. Nguyen, et al., On the simplification of cable model in static analysis of large dimension cable-driven parallel robots, in: Proceedings of IEEE International Conference on Intelligent Robots and Systems (IROS), Tokyo, November, 3–7, 2013, pp. 928–934.
[35] Kouta Kunugi, Hirohisa Kojima, Pavel M. Trivailo, Modeling of tape tether vibration and vibration sensing using smart film sensors, Acta Astronaut. 107 (2015) 97–111.
[36] Giovanni B. Palmerini, Silvano Sgubini, Marco Sabatini, Space webs based on rotating tethered formations, Acta Astronaut. 65 (1–2) (2009) 131–145.
[37] A.L. Nelson, K.W. Folley, M. Coral, Differential Equations, D. C. Heath & Co., Boston 1952, pp. 160–161.
[38] J.R. Johnson, W.M. Grundy, M.T. Lemmon, Dust depostion at the Mars Pathfinder landing site: observations and modeling of visible/near-infrared spectra, Icarus 163 (2) (2003) 330–346.
[39] K.M. Kinch, J. Sohl-Dickstein, J.F. Bell III, J.R. Johnson, W. Goetz, G.A. Landis, Dust deposition on the Mars Exploration Rover Panoramic Camera (Pancam) calibration targets, J. Geophys. Res. E: Planets 112 (6) (2007) (art. no. E06S03).
[40] J.L. Campbell, P.L. King, L. Burkemper, J.A. Berger, R. Gellert, N.I. Boyd, G. M. Perrett, I. Pradler, L. Thompson, K.S. Edgett, R.A. Yingst, The Mars Science Laboratory APXS calibration target: comparison of Martian measurements with the terrestrial calibration, Nucl. Instrum. Methods Phys. Res. Sect. B: Beam Interact. Mater. Atoms 323 (2014) 49–58.